

Photoacoustic tomography as a method to estimate the optical fluence distribution in turbid media: supplement

LAWRENCE C. M. YIP,^{1,2,†}  ELINA RASCEVSKA,^{1,3,†}  PARSA OMIDI,³  AND JEFFREY J. L. CARSON^{1,2,3,4,*}

¹Lawson Health Research Institute, Imaging Program, 268 Grosvenor St., London, Canada, N6A 4V2, Canada

²Western University, Schulich School of Medicine and Dentistry, Department of Medical Biophysics, 1151 Richmond St, London, Canada, N6A 3K7, Canada

³Western University, School of Biomedical Engineering, 1151 Richmond St, London, Canada, N6A 3K7, Canada

⁴Western University, Schulich School of Medicine and Dentistry, Department of Surgery, 1151 Richmond St, London, Canada, N6A 3K7, Canada

[†]Co-first authors

*jcarson@lawsonimaging.ca

This supplement published with Optica Publishing Group on 5 September 2023 by The Authors under the terms of the [Creative Commons Attribution 4.0 License](https://creativecommons.org/licenses/by/4.0/) in the format provided by the authors and unedited. Further distribution of this work must maintain attribution to the author(s) and the published article's title, journal citation, and DOI.

Supplement DOI: <https://doi.org/10.6084/m9.figshare.23800689>

Parent Article DOI: <https://doi.org/10.1364/BOE.496078>

PHOTOACOUSTIC TOMOGRAPHY AS A METHOD TO ESTIMATE THE OPTICAL FLUENCE DISTRIBUTION IN TURBID MEDIA: SUPPLEMENTAL DOCUMENT

1. Phantom preparation

Phantoms were fabricated using a mold depicted in Fig.S1. The mold included the mounting piece (Fig.S1., on the left) enclosed by two halves of a spherical shell (Fig.S1., middle and on the right). The mold was 3D printed using a Formlabs Form 2 printer (Formlabs, Somersville, MA). Clear (v2) and White (v1) photopolymer resins (Formlabs, Somersville, MA) were used for printing the mounting piece and spherical shell, respectively.

Before liquid agarose was poured, the mounting piece was positioned between the two spherical shells. As a precaution, the shells were held together with tape. The assembled mold was placed on a level surface to ensure a flat surface perpendicular to the illumination axis. Holes were used to set the height of the first layer (~35 mm). After the first layer was poured, the phantoms were left to rest at room temperature until solidified. Then, the level holes were sealed and the second layer of (transparent) agarose was poured until it started leaking out the top opening (~17 mm).

Once both layers solidified, the mold shells were removed, leaving the mounting piece inside the phantom. The fiber bundle for directional illumination was inserted in the opening on the mounting piece. A rod was attached to the mounting piece to extend the phantom into the water tank.

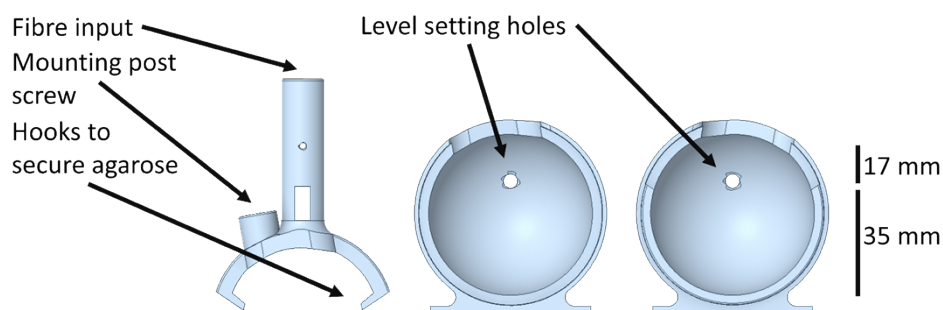


Fig. S1. Renderings of a 3D-printed phantom holder and mold. (On the left) Holder used to secure and align the phantom to the mounting post and optical fiber. (Middle) One half of the spherical shell mold. (On the right) The second half of the spherical shell mold.

2. Optical characterization of India ink

India ink is commonly used as an optical absorber in biomedical optics research, but its optical properties can suffer from variability between manufacturers and batches. Additionally, the small amounts of India ink used in this study were susceptible to experimental error due to adherence to pipette walls or inconsistencies in pipetting technique. Therefore, for each phantom, a sample of agarose and India ink mixture was taken after the desired concentration was achieved and absorbance was measured using a UV-VIS spectrophotometer (Beckman DU640, Beckman Coulter Inc., Brea, CA) at wavelengths of 680 nm, 800 nm and 930 nm. For each measurement, the spectrophotometer was blanked using a clear sample of agarose gel from the same mixture.

The absorption coefficients (μ_a) were computed using the Lambert-Beer law. It was assumed that scattering was negligible, and all attenuation resulted from absorption. The optical path length was the length of the cuvette used (10 mm).

Figure S2 shows the India ink absorption coefficient as a function of concentration for select wavelengths (680 nm, 800 nm, and 930 nm). All three wavelengths showed a good linear relationship ($R^2 > 0.997$) within the concentration range measured.

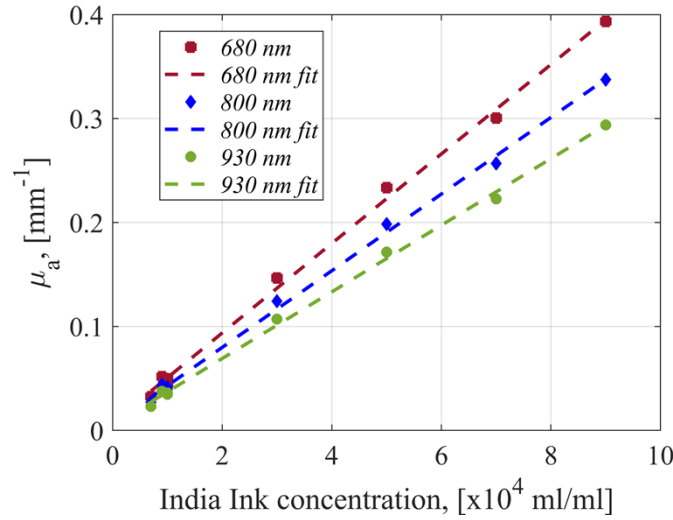


Fig. S2. Absorption coefficient (μ_a) as a function of India ink concentration at wavelengths of 680 nm, 800 nm, and 930 nm. Linear fit (dashed lines) was applied to data.

3. Optical characterization of Intralipid®

Intralipid® is a lipid emulsion commonly used to modify the optical scattering of tissue mimicking phantoms. We estimated the scattering coefficient (μ_s) using a spectrophotometric method with highly dilute samples. Intralipid® solutions of 0.2%, 0.3%, 0.4% to 0.9% (v/v) were prepared with distilled-deionized water. Stock samples of Intralipid® were shaken well prior to use. Dilution series were repeated in triplicate for two separate containers of Intralipid® within the same case. Each sample was measured in the spectrophotometer giving a total of 30 measurements across six dilution series.

The dilution series were found to be very consistent between each other with slopes averaging 39.25 with a SD of 0.97 and ($R^2=0.99$). This average slope value was used to estimate the phantom scattering properties, as well as for all other theoretical calculations and simulations as necessary.

4. Transverse line profile analysis

The optical fluence distribution widths were compared between experimental and simulated data. Transverse line profiles were taken of each PAT image and Monte Carlo simulation result at depths of 6 mm (Set A), 2.5 mm (Set B), and 1.25 mm (Set C) and the full widths at 5% of the maximum intensity (chosen to be above the noise floor of all images) were compared. Depths were chosen to maximize the differences within each phantom set. For each image, line profiles were taken for every 45° sweep around the illumination (x) axis.

In Fig. S3a, the measured average full width was plotted against the phantom absorption. For each image, the mean and standard deviation (SD) was estimated over the four-line profiles measured at 45° sweeps. For each simulated volume, the line profile widths were consistent between the four sweeps, with the maximum SD of 0.24 mm. Experimental results were generally wider than simulated results and had much higher variation between the measurement axes, as high as 6 mm. The slopes for the experimental and simulated data linear fits appeared very similar at -8.2 and -8.7, respectively. However, the linear relationship for the experimental data was very poor ($R^2=0.26$) compared to the simulated data fit of $R^2=0.93$.

In Fig. S3 (b, c), the measured average full width was plotted against the phantom scattering for set B and set C, respectively. For both simulation sets, the width measurements remained consistent across the measurement axis, varying no more than 0.2 mm (SD), while experimental data variation was high. The experimental measurement variation also increased with increasing scattering coefficient. The average deviation for set B was 11.9 mm with a maximum of 12.4 mm, increasing to 18.2 and 23.5 mm, respectively, for set C. The slopes of experimental and simulated data differed significantly for both B (0.41 and 0.91) and C (1.53 and -0.12) sets. For set B (Fig.S3b), the linear relationship of the experimental data ($R^2=0.71$) was better than with the absorbing data and, whereas the simulated data ($R^2=0.80$) was worse. Experimental data in set C (Fig.S3c) had poor linear relationship ($R^2=0.15$), while simulated data maintained a good linear fit ($R^2=0.81$).

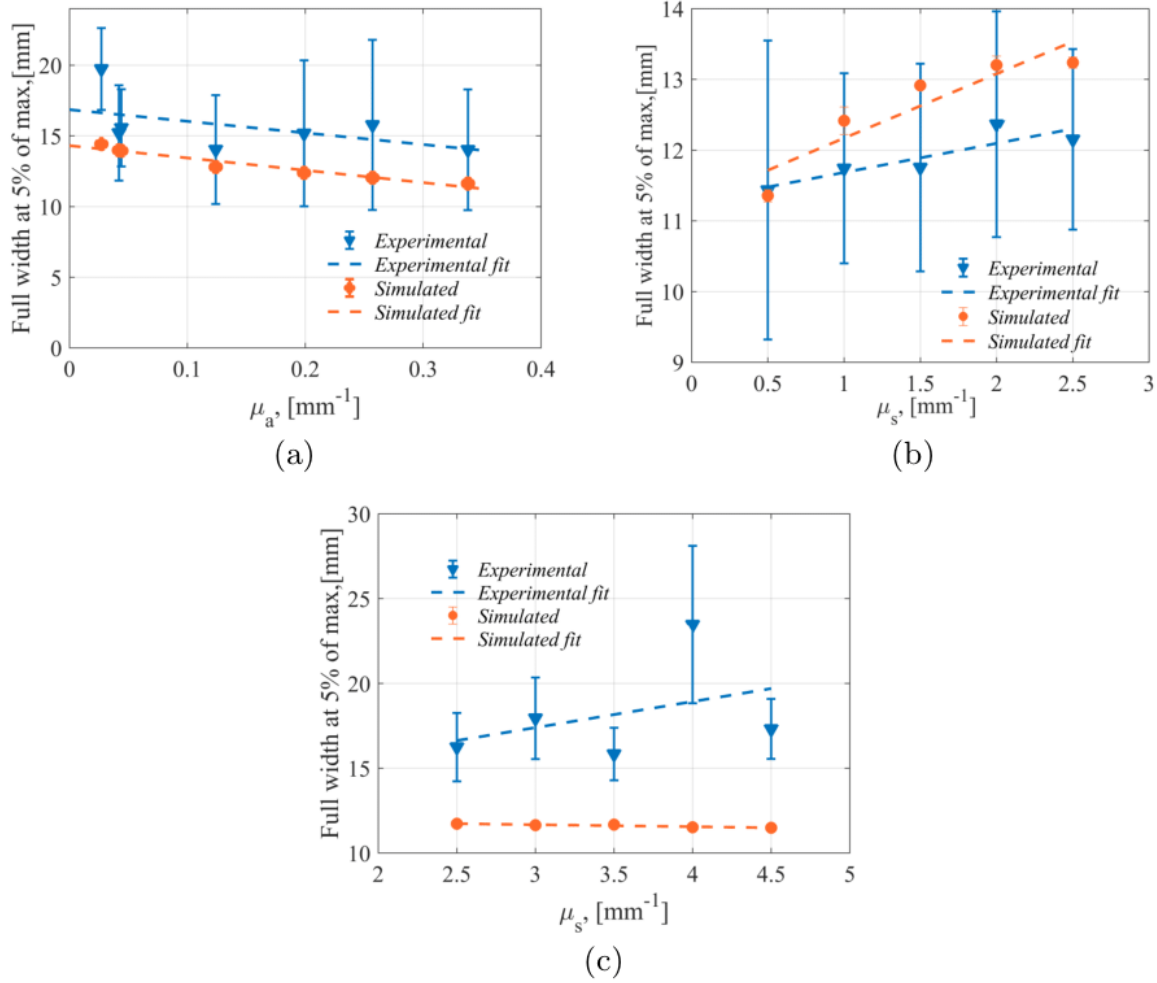
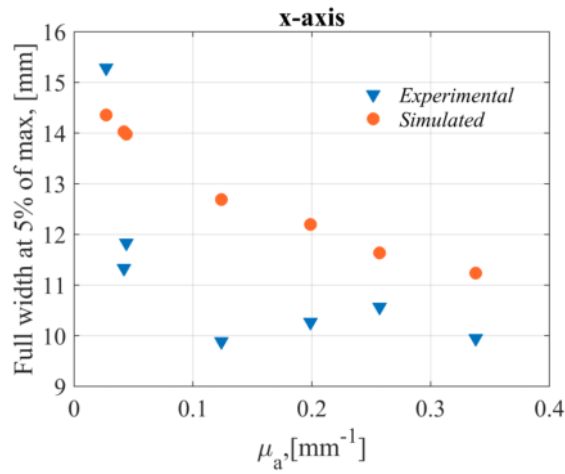


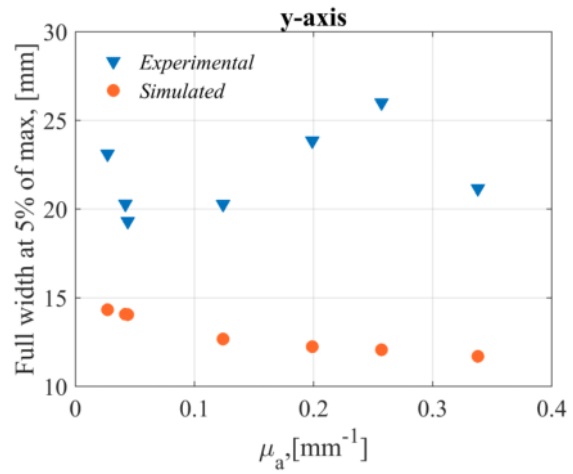
Fig. S3. Transverse line profile full widths at 5% of maximum plotted against phantom attenuation (a) Set A results. (b) Set B results. (c) Set C results. Error bars denote the SD of data in each rotated axis.

The high variation between the four angular measurements taken from the experimental image was examined more closely by looking at each individual measurement and comparing them between the locations taken, as well as against the simulated results. Figure S4 shows individual measurements for each phantom at the four angular positions (x -axis, y -axis, x -axis (45°) and y -axis (45°)). Here, it can be seen that the measurements taken at angular positions of x -axis (45°) and y -axis (45°) correlated much better to the simulated data compared to the measurements on the x - and y -axis. The highest measurement deviation from the expected can be seen at the y -axis (Fig.S4b), where it deviated from the simulated data on average by -8.90 ± 3.03 mm (SD). In comparison, the x -axis, x -axis (45°), and y -axis (45°) deviated by -1.57 ± 1.27 mm (SD), 2.30 ± 2.07 (SD), 0.76 ± 1.85 (SD), respectively.

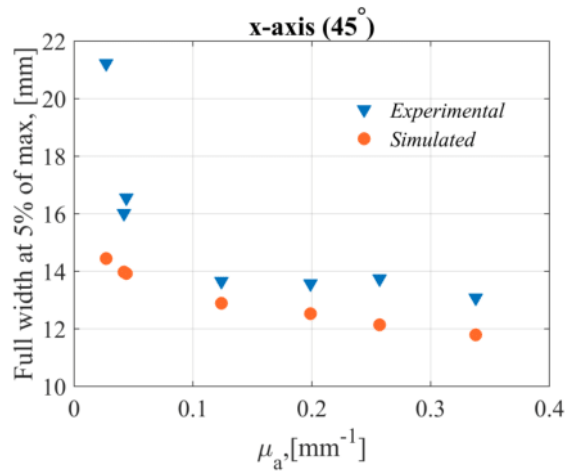
This demonstrated the isotropy of the simulated data and lack of anisotropy for the experimental data around the central illumination axis. The source of the anisotropy is likely attributable to the lack of photoacoustic sensor coverage at the location of the mounting rod and is discussed more in the discussion section of the paper.



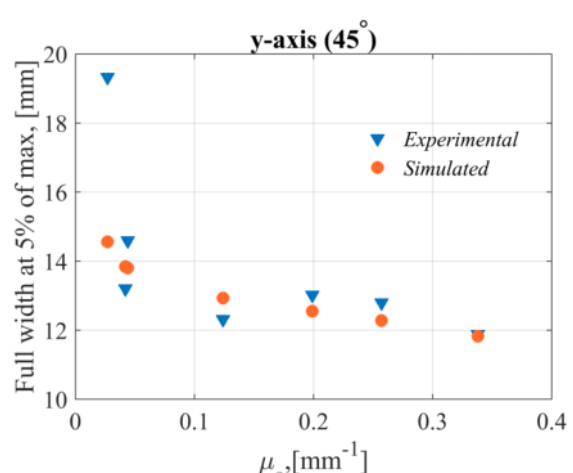
(a)



(b)



(c)



(d)

Fig. S4. Transverse line profile full widths at 5% of maximum plotted against phantom attenuation for set B. Measured full width at 5% of maximum in experimental and simulated data on (a) x-axis, (b) y-axis, (c) x-axis (45°) and (d) y-axis (45°).